JOURNAL OF SYNCHROTRON RADIATION
ISSN 1600-5775

# Quantitative three-dimensional nondestructive imaging of whole anaerobic ammonium-oxidizing bacteria

Meng-Wen Peng,[a] Yong Guan,[b] Jian-Hong Liu,[b] Liang Chen,[b] Han Wang,[a] Zheng-Zhe Xie,[c] Hai-Yan Li,[a] You-Peng Chen,[a]* Peng Liu,[d] Peng Yan,[a] Jin-Song Guo,[a] Gang Liu,[b]* Yu Shen[e] and Fang Fang[a]

[a]Key Laboratory of the Three Gorges Reservoir Region's Eco-Environments of MOE, Chongqing University, Chongqing 400045, People's Republic of China, [b]National Synchrotron Radiation Laboratory, University of Science and Technology of China, Hefei 230026, People's Republic of China, [c]i-Lab, Suzhou Institute of Nano-Tech and Nano-Bionics, Chinese Academy of Sciences, Suzhou 215123, People's Republic of China, [d]School of Environmental Studies, China University of Geosciences, Wuhan 430074, People's Republic of China, and [e]National Base of International Science and Technology Cooperation for Intelligent Manufacturing Service, Chongqing Technology and Business University, Chongqing 400067, People's Republic of China. *Correspondence e-mail: ypchen@cqu.edu.cn, liugang@ustc.edu.cn

Received 21 August 2019
Accepted 19 February 2020

Edited by R. W. Strange, University of Essex, UK

**Keywords:** synchrotron; three-dimensional nondestructive-imaging; anammox; iron.

**Supporting information**: this article has supporting information at journals.iucr.org/s

Anaerobic ammonium-oxidizing (anammox) bacteria play a key role in the global nitrogen cycle and in nitrogenous wastewater treatment. The anammox bacteria ultrastructure is unique and distinctly different from that of other prokaryotic cells. The morphological structure of an organism is related to its function; however, research on the ultrastructure of intact anammox bacteria is lacking. In this study, *in situ* three-dimensional nondestructive ultrastructure imaging of a whole anammox cell was performed using synchrotron soft X-ray tomography (SXT) and the total variation-based simultaneous algebraic reconstruction technique (TV-SART). Statistical and quantitative analyses of the intact anammox bacteria were performed. High soft X-ray absorption composition inside anammoxosome was detected and verified to be relevant to iron-binding protein. On this basis, the shape adaptation of the anammox bacteria response to iron was explored.

## 1. Introduction

Anaerobic ammonium oxidizing (anammox) bacteria are widespread bacteria in rivers (Chen *et al.*, 2019), marine sediment (van de Vossenberg *et al.*, 2013), paddy soil (Zhu *et al.*, 2011), oil fields (Li *et al.*, 2010) and wastewater treatment plants (Ali *et al.*, 2015). Anammox bacteria are estimated to account for up to 50% of the nitrogen removal from the oceans (Strous *et al.*, 2006). Moreover, the anaerobic, autotrophic anammox bacteria obtain energy from the oxidation of ammonium with nitrite to nitrogen gas (van de Vossenberg *et al.*, 2013; Zhang *et al.*, 2018, 2019). This property makes anammox bacteria suitable for the removal of nitrogen compounds from nitrogenous wastewater due to their environmental friendliness and cost-effectiveness (Innerebner *et al.*, 2007). Further, anammox bacteria are prokaryotic organisms but contain a fairly large organelle structure. Anammox bacteria have an irregular, membrane-bounded intracellular compartment called the anammoxosome (van Niftrik *et al.*, 2008*a*). The anammoxosome organelle is unique and only exists in anammox bacteria (van Niftrik *et al.*, 2008*b*). The key catabolic metabolism occurs in anammoxosome (van Niftrik *et al.*, 2008*b*; de Almeida *et al.*, 2015). In addition, anammox membranes contain unique membrane lipids called ladderanes (Neumann *et al.*, 2014). Ladderane lipids are calculated to

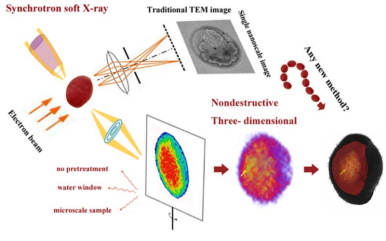

have a density of 1.5 kg $dm^{-3}$ and are unique to anammox bacteria (Damsté *et al.*, 2002). The dense membrane reduces the leakage of protons and valuable intermediates of the anammox process (Moss *et al.*, 2018). This complex biological structure makes anammox bacteria unique in terms of biological morphology.

The morphology of microbes is closely related to their function. The multicellular filamentation of *Herpetosiphon* was presumed to be associated with predatory behavior, predation defense and motility in aqueous or soil environments (Kysela *et al.*, 2016). *Caulobacter crescentus* adapts to different environmental challenges by adjusting its shape (Woldemeskel & Goley, 2017). The stalk of *Caulobacter* has been shown to elongate up to 30 µm when faced with phosphate starvation (Schmidt & Stanier, 1966) and this stalk elongation structure was hypothesized to enhance phosphate absorption (Poindexter, 1984). Moreover, *Shewanella alga BrY* adapts to starvation by reducing its cell volume from 0.48 to 0.2 $\mu m^3$; the starved cell can be resuscitated to the prior volume in a suitable environment (Caccavo *et al.*, 1996). Similar morphological changes were reported in Mn-oxidizing bacteria, *i.e. Halomonas meridiana and Marinobacter algicola* in response to Mn (II)-induced stress. Fernandes *et al.* (2018) reported that the cell length of *Halomonas meridiana and Marinobacter algicola* increased significantly to improve the Mn (II) oxidizing ability. The cell morphology of bacteria can be adapted dynamically depending on environmental conditions, a requirement for optimal survival and growth (Woldemeskel & Goley, 2017). Thus, morphology research is of great significance. However, the morphology of intact anammox bacteria has not been investigated to date and the shape adaptations of anammox bacteria under different environment conditions remain unclear.

Currently, the most effective and advanced imaging method for anammox bacteria is the transmission electron microscope (TEM) technique. In spite of the successful application of the TEM method for the analysis of the anammox structure, the limited transmission depth, the inherently low contrast and the destructive pre-treatment including dehydration, embedding and the ultrathin section (Gambelli *et al.*, 2016) has made it impossible to date to image the three-dimensional (3D) structure of intact anammox bacteria. The development of cryo-electron tomography has resulted in many breakthroughs in the imaging field (Wang *et al.*, 2017) but the method requires that the sample has to be cut into nanoscale slices (at most up to 500 nm). Limited by the weak penetration, cryo-electron tomography is incapable of high-throughput imaging for micrometre-thick cells (Milne & Subramaniam, 2009). To date, the structure of the whole anammox bacteria cell has not been determined. The lack of effective *in situ* imaging methods of whole anammox bacteria limits the further exploration of anammox bacteria. Thus, an *in situ* nondestructive method for the morphological study of intact anammox bacteria is urgently required to reveal the microstructure of anammox bacteria.

Synchrotron soft X-ray tomography (SXT) is an *in situ* nondestructive imaging technology. It provides a method to obtain a non-destructive 3D image of whole hydrous cells. Synchrotron soft X-ray photons can penetrate hydrated specimens up to 15 µm. This property permits the imaging of the entire intact anammox cell in its natural state without any staining, sectioning, dehydration or embedding pretreatments (Schneider *et al.*, 2010; Hierro-Rodriguez *et al.*, 2018). The synchrotron soft X-ray wavelength is adjustable and, by using the 'water window' range from 2.3 nm to 4.4 nm, the absorption of organics is almost an order of magnitude higher than that of water (Le Gros *et al.*, 2014), thus the organics can be distinguished from water by natural contrast at 30 nm resolution (Schneider *et al.*, 2010). In addition, this imaging method allows for obtaining the transmission image along the projection direction, as well as providing information on the interior structure of the specimen (Schneider *et al.*, 2010; Wang *et al.*, 2015). Thus, unlike other imaging methods, SXT provides a unique opportunity for imaging intact anammox cells in the *in situ* state. The synchrotron SXT technique was successfully applied to the 3D mapping of microbial cell, such as the 3D reconstruction of saccharomyces organelles (Schneider *et al.*, 2010), nanoimaging of suspended bacterial cells (Parkinson *et al.*, 2013), imaging of the structure of hepatitis C virus (HCV) replicon-harboring cells (Pérez-Berná *et al.*, 2016), and research of superparamagnetic iron oxide nanoparticle reactions with a breast cancer cell (Chiappi *et al.*, 2016). However, to date, the synchrotron SXT technique has not been applied to anammox cells; therefore, this topic requires investigation.

In this study, the synchrotron SXT technique was used to image an intact anammox bacteria cell. The total variation-based simultaneous algebraic reconstruction technique (TV-SART) was employed in this study to optimize the imaging process and obtain the image information. The linear absorption coefficient (LAC) was determined based on the TV-SART algorithm. The 3D ultrastructure of an intact anammox cell in its natural hydrous state were quantified, and the components inside anammoxosome were explored. On this basis, the shape adaptations of anammox bacteria in response to different environments were investigated.

## 2. Materials and methods

### 2.1. Cultivation and purification of the anammox granules

The anammox granules were cultivated in a 2 l expanded granular sludge blanket (EGSB) reactor (Xing *et al.*, 2017; Peng *et al.*, 2019). The reactor has been running steadily for five years and the mineral medium (per litre demineralized water) consists of $NH_4Cl$, 764 mg (200 mg $l^{-1}$ $NH_4N$); $NaNO_2$, 985 mg (200 mg $l^{-1}$ $NO_2N$); $KHCO_3$, 2.133 g; $KH_2PO_4$, 25 mg; $MgSO_4{\cdot}0.7H_2O$, 200 mg; $CaCl_2{\cdot}0.2H_2O$, 200 mg; $FeSO_4$, 0.03 m*M*; and 1 ml of trace element solution I and II as described by van de Graaf *et al.* (1996). The anammox granules extracted from the EGSB reactor were ground and dispersed by homogenizer, and washed in phosphate buffer three times. The collected biomass was treated with 0.2 m*M* EDTA and glass bead milling at 20 Hz for 30 s, and then

physically dispersed using a Vortex Mixer. Finally, the dispersed anammox bacteria were purified by Percoll density centrifugation (Strous *et al.*, 1999).

### 2.2. Diversity analysis of the anammox granules

Microbial DNA was extracted from the anammox granules in the EGSB reactor using the EZNA soil DNA kit (Omega Bio-Tek). The final DNA concentrations were determined using an ultraviolet–visible (UV–VIS) spectrophotometer (PerkinElmer Lambda 950) and the DNA molecular mass was determined by gel electrophoresis with 1% agarose. The V3–V4 regions of the anammox 16S rRNA gene were amplified with the primer 338F (5′-ACTCCTACGGGAGGCAGCAG-3′) and the primer 806R (5′-GGACTACHVGGGTWTC-TAAT-3′) using polymerase chain reaction (PCR) (ABI GeneAmp 9700). The PCR program was as follows: 3 min of denaturation at 95°C, 27 cycles of 30 s at 95°C, 30 s for annealing at 55°C, 45 s for elongation at 72°C, and a final extension at 72°C for 10 min. A mixture of 4 µl of 5 × FastPfu buffer, 2 µl of 2.5 m*M* dNTPs, 0.8 µl of 5 µ*M* 338F primer and 0.8 µl of 5 µ*M* 806R primer, 0.4 µl of FastPfu polymerase, 0.2 µl BSA and 10 ng template DNA was added to the reaction system; deionized water was added to obtain 20 µl. Two parallel PCR reactions were performed at the same time. The resulting PCR products were extracted from 2% agarose gel and further purified using the AxyPrep DNA gel extraction kit (Axygen Biosciences) and were quantified by QuantiFluor-ST (Promega). The Illumina MiSeq PE300 platform (Illumina, San Diego, USA) was used for sequencing of the purified amplicons and the raw reads were deposited into the National Center for Biotechnology Information (NCBI) Sequence Read Archive (SRA) database. The operational taxonomic units (OTUs) were clustered with a 97% similarity cutoff using *UPARSE* (version 7.1 http://drive5.com/uparse/) and the chimeric sequences were identified and removed using *UCHIME*. The taxonomy of the 16S rRNA gene sequences was analyzed using the ribosomal database project (RDP) classifier algorithm (http://rdp.cme.msu.edu/) against the Silva (SSU123) 16S rRNA database using a confidence threshold of 70%.

### 2.3. Anammox bacteria purification analysis with fluorescence *in situ* hybridization

The purified anammox bacteria were fixed with ice in 4% paraformaldehyde for 12 h and were then dehydrated in 50%, 80% and 100% ethanol for 10 min; 1 µl of probe Amx368 and 9 µl of hybridization buffer were added to the enriched anammox bacteria in the hybridization wells (Strous *et al.*, 1999; Zhang *et al.*, 2016). The probe Amx368 CCTTTCGGGCATTGCGAA labeled with Cy3 at the 5′ end was applied to determine the total anammox bacteria. The hybridization was performed in a hybaid oven at 46°C for 90 min. The total biomass of the enriched bacteria was stained with 10 µl DAPI at 5 µg ml$^{-1}$ for 15 min (Schmid *et al.*, 2003). All operations related to the fluorochromes were conducted in a dark environment to avoid fluorescence quenching. The fluorescence images of the anammox bacteria and total biomass were obtained with a confocal laser scanning microscope (CLSM) (Olympus, FV1200); the excitation wavelength of Cy3 was set at 552 nm and the DAPI dye was set at 488 nm for the CLSM analysis. The ratio of the anammox to the total biomass was determined using *Photoshop* software.

### 2.4. Imaging of the anammox bacteria

**2.4.1. Synchrotron soft X-ray 3D imaging of the anammox bacteria.** The synchrotron soft X-ray imaging experiment was performed at the BL07W beamline at the National Synchrotron Radiation Laboratory (NSRL) in Hefei, China (Zheng *et al.*, 2016). The purified anammox bacteria were centrifuged at 5000 g (Eppendorf, 5804R) for 2 min and were re-suspended in deionized water and then diluted to 1–2 × 10$^{7}$ ml$^{-1}$; 0.4 µl of the anammox bacteria suspension was seeded onto 100-mesh carbon-film copper grids. Subsequently, the cells were rapidly placed into liquid nitrogen to remain vitrified to prevent radiation damage (Schneider *et al.*, 1995). The copper grids with the purified anammox cells were transferred into the vacuum cryogenic chamber of the soft X-ray instrument for imaging; the 'water window' (0.52 keV photon energy) was used to take advantage of the high natural contrast of the organics in the 'water window' (Carrascosa *et al.*, 2009). A visible-light microscope and a soft X-ray microscope were coupled to determine the suitable samples. The anammox cells perpendicular to the beamline (at 0° tilt) were the targets for the imaging. The images were acquired at a 2 s exposure time from −65° to 65° at 1° intervals, which was achieved by rotating the sample stage. A schematic of the 3D imaging of the intact anammox cell is shown in Fig. 1. The synchrotron soft X-ray illumination was focused on the condenser and interacted with the anammox bacteria sample on the sample stage. After adsorption and scattering by the anammox bacteria, the transmission of the soft X-ray signal was amplified by a condenser zone plate and detected by the charge coupled device (CCD).

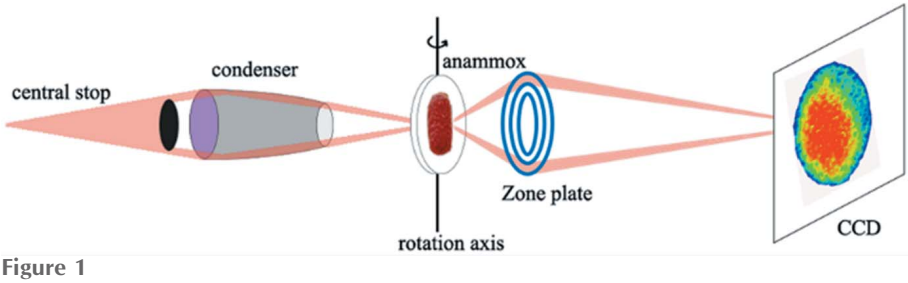


**Figure 1**
Schematic of the SXT of the anammox cell. The synchrotron soft X-ray illumination is focused on the anammox cell by the condenser. After being absorbed by the anammox cell, an enlarged imaged of the anammox cell is transmitted by the objective zone plate onto a charge-coupled device (CCD).

**2.4.2. Reconstruction and segmentation of the anammox cells**. To obtain the 3D information of the anammox ultrastructure, a tomographic reconstruction of the 131 images obtained from different angles was conducted using the FBP algorithm. Some angles were missing because of grid shading, and the algebraic reconstruction technique (ART) was used for the missing wedges. TV-SART in the *TomoJ* software was applied to obtain detailed structural information (Liang *et al.*, 2013). The reconstruction results of the TV-SART algorithm were evaluated using the LAC values. The LAC represents the inherent ability of a substance to absorb the soft X-rays (Weiss *et al.*, 2000), and the images depicting the LAC were segmented to identify the different organelle structures and chemical composition (Liu *et al.*, 2018; Sinka *et al.*, 2004). *Amira* software was used to segment the reconstructed anammox bacteria cell, calculate the LAC values, measure the number of pixels of the anammoxosome organelle and anammox bacteria cell, and to create movies (Schneider *et al.*, 2010; Uchida *et al.*, 2011).

### 2.5. Label-free proteomics analysis

**2.5.1. Protein extraction and digestion**. The anammoxosome organelles were isolated according to the previous report (Damsté *et al.*, 2002). Then the collected anammoxosome pellets were re-suspended in a phosphate buffer solution with the protease inhibitor phenylmethanesulfonyl fluoride (PMSF). Then, the suspension was rotated for 12 h and centrifuged at 300 g at 8°C to collect the supernatants. The collected supernatants were centrifuged at 14000 g at 4°C for 5 min to collect the sediment. The precipitated bacteria pellets were washed with PBS twice, re-suspended with a lysis buffer (1% SDS, 8 *M* urea, PMSF), and sonicated for 2 min. Following incubation on ice for 30 min, the lytic bacteria were centrifuged at 14000 g for 30 min at 4°C and the supernatants were collected. Subsequently, 90% of precooled acetone was added, followed by precipitation for 12 h at −20°C. The solutions were centrifuged and the supernatants were discarded. The sediment was re-suspended with a lysis buffer (1% SDS, 8 *M* urea cocktail), followed by centrifugation at 12000 g at 4°C for 20 min; the supernatants were collected and the total protein was extracted and separated using polyacrylamide gel electrophoresis (PAGE). Protein digestion was conducted using the standard procedure (Wiśniewski *et al.*, 2009). In general, 150 µg of protein was transferred to the centrifuge tube and replenished with a pyrolysis solution to 135 µl. Tris(2-carboxyethyl)phosphine was added to the final concentration of 10 m*M* and the tubes were incubated at 37°C for 60 min. Then 100 µl of 50 m*M* iodoacetamide was added to the tube and incubated for 20 min in darkness. Cold acetone at six times the volume of the sample was added to the tube and incubated at −20°C for 4 h. The acetone was discarded at 10000 rpm for 20 min and the sediment was re-suspended with 200 µl TEAB buffer at 100 m*M*. Then, 3.0 µg of trypsin solution was added and incubated overnight at 37°C. The quantification of the peptide concentrations was conducted using the Peptide Quantitative kit (Thermo).

**2.5.2. Liquid chromatography–mass spectrometry of the total protein**. Peptides were injected into a mass spectrometer (MS; Q Exactive) coupled with a nanoliquid chromatography instrument (Easy-nLC 1200), and peptide separation was achieved on a C18 reversed-phase column (4.6 mm × 150 mm, 5 µm Thermo, USA). The mobile phase A was 2% acetonitrile and 0.1% formic acid in water and the mobile phase B was 80% acetonitrile and 0.1% formic acid in water. The flow rate was 300 nl $min^{-1}$. The following gradient elution was applied: 0–1.0 min, 0–5% B; 1.0–41.0 min, 5–23% B; 41.0–51.0 min, 23–29% B; 51.0–59.0 min, 29–100% B; 59.0–65.0 min, 100% B; and 65.0–90 min, 100% B. The flow rate was 0.8 ml $min^{-1}$. The spray voltage of the MS was 1.8 kV. The MS was operated in data-dependent mode to automatically switch between MS and tandem MS/MS acquisition. The spray voltage of the MS was 1.8 kV. The full-scan range from $m/z$ 350 to 1300 was acquired with a mass resolution of 70000, followed by 20 sequential high-energy collisional dissociations (HCD). Tandem MS/MS scans with a resolution of 17500 were performed using a dynamic exclusion of 18 s.

### 2.6. Morphological characteristics of the anammox bacteria response to $Fe^{2+}$

To explore the shape adaptation and mechanism of the anammox bacteria response to different iron conditions, batch tests were performed using 120 ml serum bottles. 2 g of the anammox granules and 100 ml of the medium were added to the serum bottle. The medium content was the same as the EGSB medium except that the ammonium and nitrite were 100 mg $l^{-1}$ and the concentrations of $FeSO_4$ were 0, 0.015, 0.03 and 0.06 m*M* in different serum bottles, respectively. The medium in the serum bottle was aerated with argon for 10 min to ensure that the dissolved oxygen concentration was below 0.02 mg $l^{-1}$. The serum bottles were incubated in a shaking bath at 30°C and 120 rpm. The medium in the serum bottle was refilled every 24 h.

## 3. Results and discussion

### 3.1. Characteristics of anammox bacteria

The anammox granules sampled from the EGSB reactor are shown in Fig. S1 of the supporting information. The round granules were deep red and the diameter range was 1.2 mm to 6.0 mm. The microbial diversity analysis of the anammox granules at the genus level is shown in Fig. 2(*a*). The anammox bacteria included three genera: *Candidatus Jettenia*, *Candidatus Brocadia* and *Candidatus Kuenenia*, accounting for 26.36%, 4.22% and 1.40% of the total microbial biomass in the EGSB reactor, respectively. Although three genera of anammox bacteria were observed in the reactor, these three genera of *Candidatus Jettenia*, *Candidatus Brocadia* and *Candidatus Kuenenia* had similar structural characteristics, including three separate compartments: periplasm, cytoplasm and anammoxosome. Furthermore, the anammoxosome volume ratio in these three genera accounted for more than

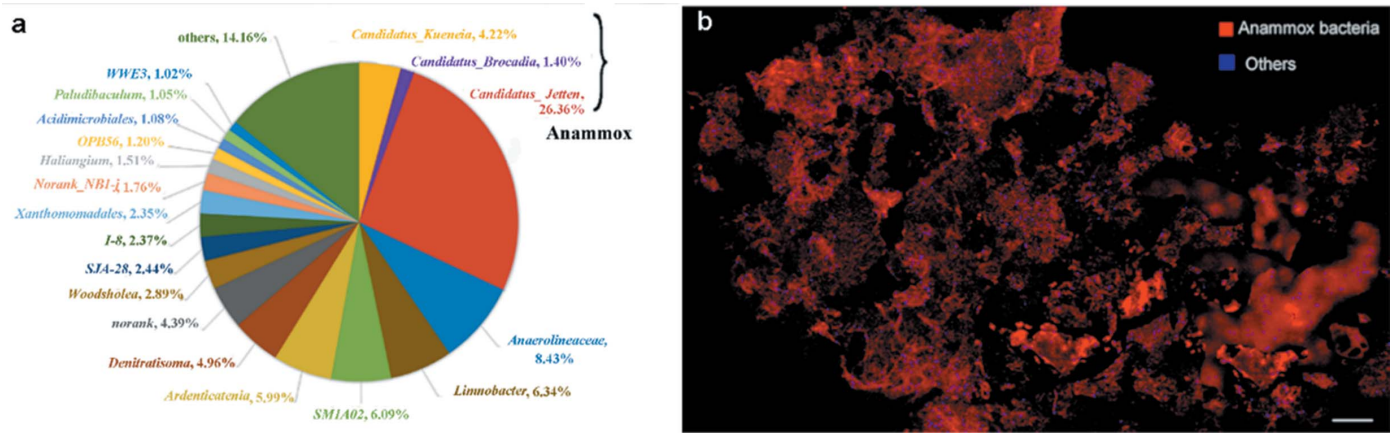


**Figure 2**
The anammox granules in the EGSB reactor. (*a*) Microbial diversity analysis of the anammox granules. (*b*) Confocal laser scanning microscope image of the anammox granules. (Scale bar shows 200 µm.) (The probe Amx368 targeting the anammox bacteria is shown in red and the DAPI dye targeting the total biomass minus the anammox bacteria is shown in blue.)

60% of the anammox bacteria volume (van Niftrik *et al.*, 2008*b*).

To further improve the purity of anammox bacteria, Percoll density gradient centrifugations were performed. The purity of anammox bacteria was detected by fluorescence *in situ* hybridization, and the CLSM image is shown in Fig. 2(*b*). The red fluorescence of anammox bacteria account for up to 95% of total fluorescence, which indicated the success of the purification of anammox bacteria.

### 3.2. Synchrotron soft X-ray imaging and reconstruction of anammox bacteria

Fig. S2 of the supporting information shows the synchrotron soft X-ray projection image of the intact cells; 131 projection images of the anammox bacteria at different angles were collected, and the 3D structure of the anammox bacteria was reconstructed using the FBP algorithm in the original soft X-ray microscopy system as shown in Supplementary Movie 1. Fig. S3(*a*) shows a screenshot of the anammox bacteria. The structure inside the anammox bacteria was inferred to be anammoxosome. Slice images of the anammox bacteria are shown in Fig. S3(*b*) and a tomogram of the anammox bacteria is shown in Supplementary Movie 2. The soft X-ray absorption of all areas inside the anammox bacteria can be visualized and the greyscale difference is shown in the slice image.

To further investigate the interior ultrastructure of the anammox bacteria, the TV-SART (Liang *et al.*, 2013) algorithm was used to reconstruct the anammox bacteria. The anammox bacteria in Fig. S3 have a strong and heterogeneous high-absorption structure but the absorption difference inside the high-absorption membrane could not be distinguished due to limitations of the FBP algorithm. In addition, some artifacts were observed in the greyscale 3D reconstruction video (Supplementary Movie 1) and were attributed to missing angles. The TV-SART algorithm can compensate for these drawbacks and provides the LAC values.

The soft X-ray absorption of the specimen follows the Beer–Lambert law (Parkinson *et al.*, 2013). The LAC values represent the soft X-ray absorption intensity, and can be calculated using the following equation (Weiss *et al.*, 2000),

$$\int_L \mu(x)\,\mathrm{d}x = \ln(I_0/I), \tag{1}$$

where $I_0$ is the initial X-ray intensity and $I$ is the output X-ray intensity. $\mu(x)$ is the local LAC value, which can be calculated by an iterative reconstruction using the TV-SART algorithm (Liu *et al.*, 2018).

The LAC value was determined based on the mass absorption coefficient and the density of the composition, as defined in the following equation,

$$\mu = \mu_\mathrm{m}\,\rho, \tag{2}$$

where $\mu$ is the LAC, $\mu_\mathrm{m}$ is the mass absorption coefficient and $\rho$ is the density of the composition. Therefore, an area with a high LAC value is an area with a high mass absorption coefficient or high density (Weiss *et al.*, 2000; Le Gros *et al.*, 2005).

Fig. 3 shows the reconstructed anammox bacteria cell at different rotation angles with 60° intervals, and a movie of the intact anammox bacteria reconstructed with the TV-SART algorithm is shown in Supplementary Movie 3. The colormap ranges from 0 to 0.46 and represents the LAC value corresponding to the differences in the structure or composition. The LAC reconstruction provided a clearer representation of the ultrastructure of the anammox bacteria. The cluster (in yellow) inside the anammoxosome membrane had a higher LAC value and some nanoparticles (in green) had extremely high LAC values (Fig. 3). Fig. 4 shows a slice image of the anammox bacteria at different depths from 100 nm to 800 nm, and the black arrows in Fig. 4 indicate the nanoparticles with extremely high LAC values. A tomograph of the anammox bacteria reconstructed with the TV-SART algorithm is shown in Supplementary Movie 4. The slice image and video show the LAC values of all areas inside the anammox bacteria. It is noteworthy that there is some high LAC composition in anammoxosome, and some nanoparticles with extremely high LAC values, up to 0.46.

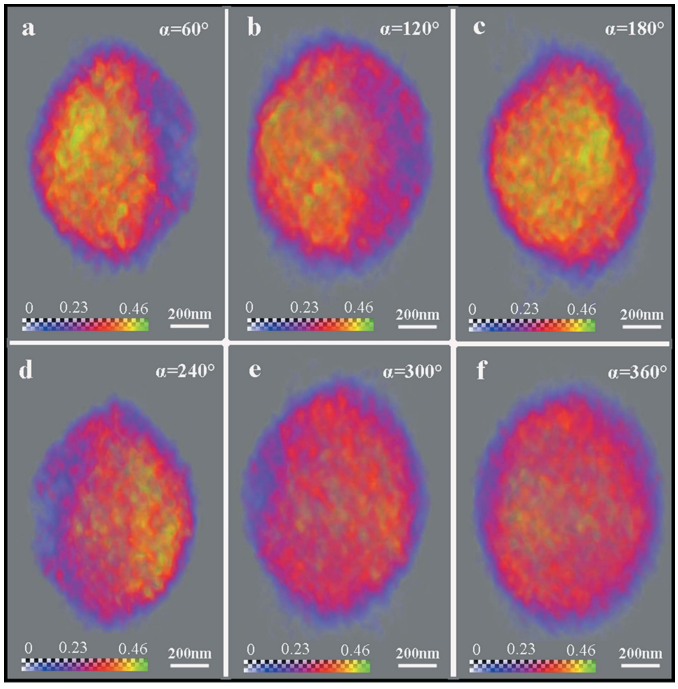


**Figure 3**
The intact anammox cell reconstructed using the TV-SART algorithm within the LAC from 0 to 0.46 (from purple to yellow). 3D reconstructions of anammox bacteria at different rotation angles at 60° intervals. Panels (*a*), (*b*), (*c*), (*d*), (*e*) and (*f*) correspond to 60°, 120°, 180°, 240°, 300° and 360°, respectively.

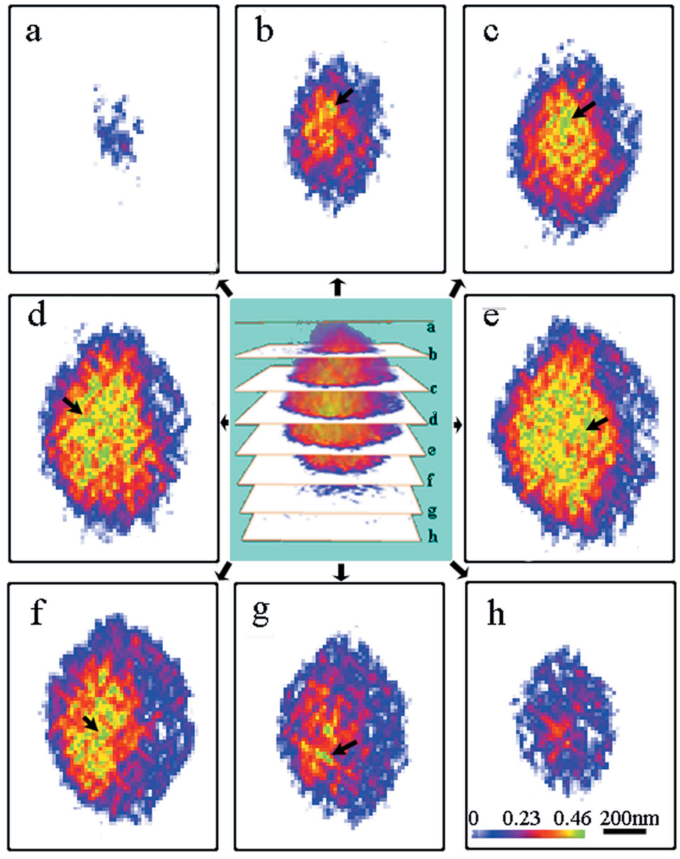


**Figure 4**
Slice images of the anammox bacteria cell at different depths. Panels (*a*), (*b*), (*c*), (*d*), (*e*), (*f*), (*g*) and (*h*) correspond to slice depths at 100 nm, 200 nm, 300 nm, 400 nm, 500 nm, 600 nm, 700 nm and 800 nm, respectively The black arrows point to nanoparticles in green. The scale bar and colormap in (*h*) apply to all images.

### 3.3. Quantitative and statistical analysis of the anammox bacteria

Since different biochemical components have specific LAC values, the organelles and other cell structures can be distinguished visually based on the differences in the biochemical composition and density (Le Gros *et al.*, 2005; Weiss *et al.*, 2000; Uchida *et al.*, 2011). Thus, the image of the ultrastructure of the anammox cell was segmented based on the local LAC values using the *Amira* software. Segmentation images of the anammox structure at different rotation angles are shown in Fig. 5, and in Figs. S4 and S5 and in a video of the segmentation of the 3D structure in Supplementary Movie 5. The 3D segmentation structure of the anammox cell showed a distinct asymmetric structure, especially at the rotation angles of 60° and 240° [Figs. 5(*a*) and 5(*d*)]. To quantify the exact position of the anammoxosome in the anammox cell, the parameter of eccentricity (*e*) was defined. Eccentricity is defined as the ratio of the longest distance to the shortest distance from the anammoxosome membrane to the cell membrane. The maximum and minimum eccentricity values of the anammoxosome are shown in Fig. S6. The average eccentricity is 3.25 ± 0.43 (Fig. S7); this demonstrates the extent to which anammoxosome deviates from the center of the anammox bacteria. Furthermore, the ratio of anammoxosome volume to the anammox bacteria cell volume (A/C) was statistical. The average A/C value was 47 ± 2.5% (Fig. S7), which was much lower than the previously reported volume ratio of 50–80% with a large average error (van Niftrik *et al.*, 2008*b*). The previous value of volume ratio was based on the area ratio of a nanoscale slice in a TEM ultrathin section (van Niftrik *et al.*, 2008*b*). However, the values of A/C varied widely due to the exocentric anammoxosome structure. Thus, the results of the anammoxosome volume ratio obtained by synchrotron soft X-ray imaging is closer to reality than that obtained by TEM.

The average LAC values of the anammox cell, the anammoxosome and the nanoparticles were calculated to be 0.326 ± 0.001 $\mu m^{-1}$, 0.389 ± 0.001 $\mu m^{-1}$ and 0.460 ± 0.001 $\mu m^{-1}$, respectively. The LAC value of the anammoxosome is much higher than that of the yeast organelles. The average LAC values of the chondriosome, vacuole, cell nucleus and nucleoli were in the ranges 0.34–0.38, 0.14–0.29, 0.25–0.27 and 0.32–0.34 $\mu m^{-1}$, respectively (Uchida *et al.*, 2011), and the LAC value of the nucleoid for various cells was 0.25 $\mu m^{-1}$ (Hammel *et al.*, 2016). The extremely high LAC value of the anammoxosome organelle indicated that the biochemical composition and structure of the anammoxosome were denser than that of the conventional organelles. Studies have shown that the anammox membrane contains abundant dense ladderane lipids with 1.5 g $cm^{-3}$ density (Damsté *et al.*, 2002), resulting in higher LAC values of anammoxosome membrane than those of the cytoplasm. The higher LAC

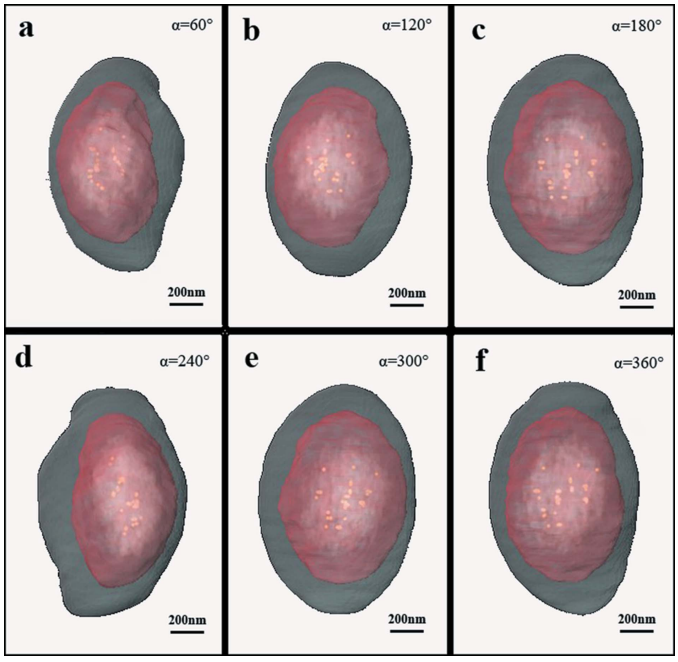


**Figure 5**
Segmentation images of the anammox cell at different rotation angles. Panels (*a*), (*b*), (*c*), (*d*), (*e*), and (*f*) correspond to 60°, 120°, 180°, 240°, 300° and 360°, respectively. $\alpha$ represents the rotation angle.

values inside the anammoxosome membrane may be related to the numerous enzymes inside the anammoxosome, as the anammoxosome is the site of the anammox reaction that is associated with the presence of many enzymes, such as hydrazine dehydrogenase (HDH), hydrazine synthase (HZS) and hydroxylamine/hydrazine oxidoreductase (HAO/HZO) (de Almeida *et al.*, 2015; van Niftrik *et al.*, 2008*a*).

### 3.4. High soft-X ray absorption components in anammoxosome

To further explore the high soft X-ray absorption components in anammoxosome, proteomics analysis of the anammoxosome was performed to explore the detailed composition in anammoxosome organelles. A large number of proteins were detected, and the identified proteins are listed in Table S1. More than half of the proteins in anammoxosome were metal-binding proteins, and 48.05% of the identified proteins were iron-binding protein, including some enzymes regulating the anammox process, such as nitrite oxidoreductase of Q1PZD8, hydrazine dehydrogenase of Q1PW30 and hydrazine synthase of Q1Q0T2 and Q1Q0T4. In addition, other metalloproteins were also detected, such as magnesium ion binding protein of I3IJ16, and magnesium and potassium binding protein of A0A1V4AVC2. Furthermore, some iron storage proteins of Q1Q315 and Q1Q5F8, which have strong capacity to store iron, were also existing in anammoxosome. These abundant proteins and the binding metal ions with high density have higher soft X-ray absorption, thus resulting in higher LAC value in anammoxosome.

### 3.5. Morphological analysis of the anammox bacteria response to $Fe^{2+}$

As iron is abundant in anammoxosome and plays an important role in the anammox process as iron-binding enzymes, the shapeshifting and mechanism of anammox bacteria response to iron were investigated in this study. Fig. 6(*a*) shows the average ratio of the anammoxosome volume to the anammox bacteria cell volume (A/C) at 0, 0.015, 0.03 and 0.06 m*M* $FeSO_4$, respectively. It was evident that the A/C volume ratio decreased with increasing iron concentration from 0 to 0.06 m*M*. The increased A/C ratio was the most characteristic shape adaptation response of the anammox bacteria to $Fe^{2+}$ starvation. An increase in the A/C ratio resulted in a larger surface area of the anammoxosome. Further, the larger surface area increased the number of metal binding sites (Antony *et al.*, 2011). Thus, the shapeshifting of the anammox bacteria due to the increased A/C ratio at lower iron concentrations was presumed to enhance the iron absorption in the face of iron starvation. This shapes adapta-

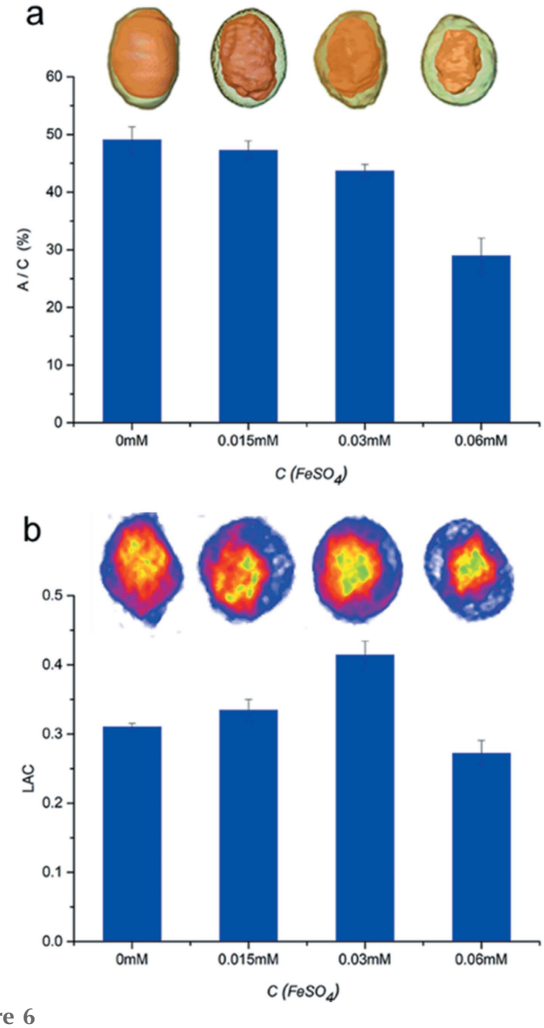


**Figure 6**
The effect of $Fe^{2+}$ on the morphology of anammox bacteria. (*a*) The average A/C volume ratio at iron concentrations of 0, 0.015 m*M*, 0.03 m*M* and 0.06 m*M*. (*b*) LAC values at iron concentrations of 0, 0.015 m*M*, 0.03 m*M* and 0.06 m*M*.

tion mechanism is similar to that of the Mn-oxidizing bacteria *Halomonas meridiana* and *Marinobacter algicola*, which adapt to Mn(II)-induced stress by increasing the cell length and volume to achieve better Mn(II) oxidizing ability (Fernandes *et al.*, 2018). Accordingly, the LAC value changed with the A/C volume ratio [Fig. 6(*b*)]. In the absence of $FeSO_4$ and in the presence of 0.015 m*M* $FeSO_4$, the LAC value of the anammoxosome was 0.220 and 0.301, respectively, representing 43% and 23% decreases in the LAC value compared with the control group at 0.03 m*M* $FeSO_4$. This may be related to two factors: one is the increase in the anammoxosome volume, which, in turn, leads to a decrease in the density of the anammoxosome; the other factor may relate to the decrease of the synthesis of iron-binding protein, and the decrease of iron storage in bacterioferritin of Q1Q315 and Q1Q4F8 in the iron deficiency environment. However, 0.06 m*M* $FeSO_4$ resulted in a decrease of the LAC value; this indicated that excessive iron was not beneficial to the synthesis of iron-binding protein. The concentration of 0.03 m*M* $FeSO_4$ might be a more appropriate concentration for anammox bacteria. A similar response of anammox bacteria to iron has previously been observed using the TEM method (Zhang *et al.*, 2009). An increase in the iron concentration from 0.03 m*M* to 0.075 m*M* resulted in lower electron absorption density and decreased area of the anammoxosome (Zhang *et al.*, 2009). This indicates the sensitivity and dependence of anammox bacteria to iron, and proved that the high X-ray absorption components was highly relevant to iron. In future studies, we will investigate this mechanism of iron regulation in anammox bacteria in detail.

## 4. Conclusion

Taken together, in this study, the SXT imaging coupled with TV-SART reconstruction was used in the morphology research of anammox bacteria for the first time. This method provided high-contrast and high-resolution 3D images of the whole anammox bacteria cell in its natural state. The ultrastructure of the anammox bacteria was imaged and quantified. The components with high X-ray absorption in anammoxosome were verified to be highly relevant to iron and iron-binding proteins, and the shape responses of the anammox bacteria to $Fe^{2+}$ were sensitive.

## Acknowledgements

The authors gratefully acknowledge Bing-Hong Wan for guidance on using the Amira software, and the BL07W beamline at the National Synchrotron Radiation Laboratory in Hefei, China; and the support of Majorbio, China.

## Funding information

Funding for this research was provided by: National Natural Science Foundation of China (award No. 21876016 to You-Peng Chen; award No. 51578527 to You-Peng Chen); Chongqing Science and Technology Commission (award No. cstc2018jcyjAX0366 to You-Peng Chen; award No. cstc2018jcyjAX0638 to Yu Shen); Fundamental Research Funds for the Central Universities (award No. 2018CDQYCH0028 to You-Peng Chen; award No. 2019CDCGHS311 to You-Peng Chen); the National Key Research & Development Program of China (award No. 2016YFE0205600 to Yu Shen).

## References

Ali, M., Oshiki, M., Awata, T., Isobe, K., Kimura, Z., Yoshikawa, H., Hira, D., Kindaichi, T., Satoh, H., Fujii, T. & Okabe, S. (2015). *Environ. Microbiol.* **17**, 2172–2189.

Almeida, N. M. de, Neumann, S., Mesman, R. J., Ferousi, C., Keltjens, J. T., Jetten, M. S., Kartal, B. & van Niftrik, L. (2015). *J. Bacteriol.* **197**, 2432–2441.

Antony, R., Sujith, P. P., Fernandes, S. O., Verma, P., Khedekar, V. D. & Loka Bharathi, P. A. (2011). *Curr. Microbiol.* **62**, 840–849.

Caccavo, F., Ramsing, N. B. & Costerton, J. W. (1996). *Appl. Environ. Microbiol.* **62**, 4678–4682.

Carrascosa, J. L., Chichón, F. J., Pereiro, E., Rodríguez, M. J., Fernández, J. J., Esteban, M., Heim, S., Guttmann, P. & Schneider, G. (2009). *J. Struct. Biol.* **168**, 234–239.

Chen, L. M., Liu, S. T., Chen, Q., Zhu, G. B., Wu, X., Wang, J. W., Li, X. F., Hou, L. J. & Ni, J. R. (2019). *Sci. Total Environ.* **665**, 171–180.

Chiappi, M., Conesa, J. J., Pereiro, E., Sorzano, C. O. S., Rodríguez, M. J., Henzler, K., Schneider, G., Chichón, F. J. & Carrascosa, J. L. (2016). *J. Nanobiotechnol*, **14**, 15.

Fernandes, S. O., Surya Prakash, L., Balan Binish, M., Padinchati Krishnan, K. & John Kurian, P. (2018). *J. Basic Microbiol.* **58**, 390–402.

Gambelli, L., Cremers, G., Mesman, R., Guerrero, S., Dutilh, B. E., Jetten, M. S. M., Op den Camp, H. J. M. & van Niftrik, L. (2016). *Front. Microbiol.* **7**, 15.

Graaf, A. A. van de, de Bruijn, P., Robertson, L. A., Jetten, M. S. M. & Kuenen, J. G. (1996). *Microbiology*, **142**, 2187–2196.

Hammel, M., Amlanjyoti, D., Reyes, F. E., Chen, J. H., Parpana, R., Tang, H. Y. H., Larabell, C. A., Tainer, J. A. & Adhya, S. (2016). *Sci. Adv.* **2**, e1600650.

Hierro-Rodriguez, A., Gürsoy, D., Phatak, C., Quirós, C., Sorrentino, A., Álvarez-Prado, L. M., Vélez, M., Martín, J. I., Alameda, J. M., Pereiro, E. & Ferrer, S. (2018). *J. Synchrotron Rad.* **25**, 1144–1152.

Innerebner, G., Insam, H., Franke-Whittle, I. H. & Wett, B. (2007). *Syst. Appl. Microbiol.* **30**, 408–412.

Kysela, D. T., Randich, A. M., Caccamo, P. D. & Brun, Y. V. (2016). *PLoS Biol.* **14**, e1002565.

Le Gros, M. A., McDermott, G., Cinquin, B. P., Smith, E. A., Do, M., Chao, W. L., Naulleau, P. P. & Larabell, C. A. (2014). *J. Synchrotron Rad.* **21**, 1370–1377.

Le Gros, M. A., McDermott, G. & Larabell, C. A. (2005). *Curr. Opin. Struct. Biol.* **15**, 593–600.

Li, H., Chen, S., Mu, B. Z. & Gu, J. D. (2010). *Microb. Ecol.* **60**, 771–783.

Liang, Z., Guan, Y., Liu, G., Bian, R., Zhang, X., Xiong, Y. & Tian, Y. (2013). *Proc. SPIE*, **8851**, 885113.

Liu, J., Li, F., Chen, L., Guan, Y., Tian, L., Xiong, Y., Liu, G. & Tian, Y. (2018). *J. Microsc.* **270**, 64–70.

Milne, J. L. S. & Subramaniam, S. (2009). *Nat. Rev. Microbiol.* **7**, 666–675.

Moss, F. R., Shuken, S. R., Mercer, J. A. M., Cohen, C. M., Weiss, T. M., Boxer, S. G. & Burns, N. Z. (2018). *Proc. Natl Acad. Sci. USA*, **115**, 9098–9103.

Neumann, S., Wessels, H. J. C. T., Rijpstra, W. I. C., Sinninghe Damsté, J. S., Kartal, B., Jetten, M. S. M. & van Niftrik, L. (2014). *Mol. Microbiol.* **94**, 794–802.

Niftrik, L. van, Geerts, W. J. C., van Donselaar, E. G., Humbel, B. M., Webb, R. I., Fuerst, J. A., Verkleij, A. J., Jetten, M. S. M. & Strous, M. (2008*b*). *J. Bacteriol.* **190**, 708–717.
Niftrik, L. van, Geerts, W. J. C., van Donselaar, E. G., Humbel, B. M., Yakushevska, A., Verkleij, A. J., Jetten, M. S. M. & Strous, M. (2008*a*). *J. Struct. Biol.* **161**, 401–410.
Parkinson, D. Y., Epperly, L. R., McDermott, G., Le Gros, M. A., Boudreau, R. M. & Larabell, C. A. (2013). *Methods Mol. Biol.* **950**, 457–481.
Peng, M.., Yu, X.., Guan, Y., Liu, P., Yan, P., Fang, F., Guo, J. & Chen, Y. (2019). *ACS Nano*, **13**, 14500–14510.
Pérez-Berná, A. J., Rodríguez, M. J., Chichón, F. J., Friesland, M. F., Sorrentino, A., Carrascosa, J. L., Pereiro, E. & Gastaminza, P. (2016). *ACS Nano*, **10**, 6597–6611.
Poindexter, J. S. (1984). *Arch. Microbiol.* **138**, 140–152.
Schmid, M., Walsh, K., Webb, R., Rijpstra, W. I., van de Pas-Schoonen, K., Verbruggen, M. J., Hill, T., Moffett, B., Fuerst, J., Schouten, S., Sinninghe Damsté, J. S., Harris, J., Shaw, P., Jetten, M. & Strous, M. (2003). *Syst. Appl. Microbiol.* **26**, 529–538.
Schmidt, J. M. & Stanier, R. Y. (1966). *J. Cell Biol.* **28**, 423–436.
Schneider, G., Guttmann, P., Heim, S., Rehbein, S., Mueller, F., Nagashima, K., Heymann, J. B., Müller, W. G. & McNally, J. G. (2010). *Nat. Methods*, **7**, 985–987.
Schneider, G., Niemann, B., Guttmann, P., Rudolph, D. & Schmah, G. (1995). *Synchrotron Radiat. News*, **8**, 19–28.
Sinka, I. C., Burch, S. F., Tweed, J. H. & Cunningham, J. C. (2004). *Int. J. Pharm.* **271**, 215–224.
Sinninghe Damsté, J. S., Strous, M., Rijpstra, W. I. C., Hopmans, E. C., Geenevasen, J. A. J., van Duin, A. C. T., van Niftrik, L. A. & Jetten, M. S. M. (2002). *Nature*, **419**, 708–712.
Strous, M., Fuerst, J. A., Kramer, E. H. M., Logemann, S., Muyzer, G., van de Pas-Schoonen, K. T., Webb, R., Kuenen, J. G. & Jetten, M. S. M. (1999). *Nature*, **400**, 446–449.
Strous, M., Pelletier, E., Mangenot, S., Rattei, T., Lehner, A., Taylor, M. W., Horn, M., Daims, H., Bartol-Mavel, D., Wincker, P., Barbe, V., Fonknechten, N., Vallenet, D., Segurens, B., Schenowitz-Truong, C., Médigue, C., Collingro, A., Snel, B., Dutilh, B. E., Op den Camp, H. J. M., van der Drift, C., Cirpus, I., van de Pas-Schoonen, K. T., Harhangi, H. R., van Niftrik, L., Schmid, M., Keltjens, J., van de Vossenberg, J., Kartal, B., Meier, H., Frishman, D., Huynen, M. A., Mewes, H., Weissenbach, J., Jetten, M. S. M., Wagner, M. & Le Paslier, D. (2006). *Nature*, **440**, 790–794.
Uchida, M., Sun, Y., McDermott, G., Knoechel, C., Le Gros, M. A., Parkinson, D., Drubin, D. G. & Larabell, C. A. (2011). *Yeast*, **28**, 227–236.
Vossenberg, J. van de, Woebken, D., Maalcke, W. J., Wessels, H. J. C. T., Dutilh, B. E., Kartal, B., Janssen-Megens, E. M., Roeselers, G., Yan, J., Speth, D., Gloerich, J., Geerts, W., van der Biezen, E., Pluk, W., Francoijs, K.-J., Russ, L., Lam, P., Malfatti, S. A., Tringe, S. G., Haaijer, S. C. M., Op den Camp, H. J. M., Stunnenberg, H. G., Amann, R., Kuypers, M. M. M. & Jetten, M. S. M. (2013). *Environ. Microbiol.* **15**, 1275–1289.
Wang, L., Zhang, T., Li, P., Huang, W., Tang, J., Wang, P., Liu, J., Yuan, Q., Bai, R., Li, B., Zhang, K., Zhao, Y. & Chen, C. (2015). *ACS Nano*, **9**, 6532–6547.
Wang, X., Li, S. H., Zhu, L., Nian, Q. G., Yuan, S., Gao, Q., Hu, Z., Ye, Q., Li, X. F., Xie, D. Y., Shaw, N., Wang, J., Walter, T. S., Huiskonen, J. T., Fry, E. E., Qin, C. F., Stuart, D. I. & Rao, Z. (2017). *Nat. Commun.* **8**, 9.
Weiss, D., Schneider, G., Niemann, B., Guttmann, P., Rudolph, D. & Schmahl, G. (2000). *Ultramicroscopy*, **84**, 185–197.
Wiśniewski, J. R., Zougman, A., Nagaraj, N. & Mann, M. (2009). *Nat. Methods*, **6**, 359–362.
Woldemeskel, S. A. & Goley, E. D. (2017). *Trends Microbiol.* **25**, 673–687.
Xing, H., Wang, H., Fang, F., Li, K., Liu, L., Chen, Y. & Guo, J. (2017). *Environ. Technol.* **38**, 1184–1190.
Zhang, L., Zheng, P. & Hu, A. H. (2009). *Acta Sci. Circumstantiae*, **29**, 1629–1634.
Zhang, Z., Gong, Z., Liu, S. & Ni, J. (2016). *Chem. Eng. J.* **287**, 529–536.
Zhang, Z. Z., Cheng, Y. F., Liu, Y. Y., Zhang, Q., Zhu, B. Q. & Jin, R. C. (2019). *Environ. Int.* **124**, 501–510.
Zhang, Z. Z., Cheng, Y. F., Xu, L. Z. J., Bai, Y. H. & Jin, R. C. (2018). *Bioresour. Technol.* **259**, 10–17.
Zheng, Z., Tang, A., Guan, Y., Chen, L., Wang, F., Chen, P., Wang, W., Luo, Y., Tian, Y. & Liang, G. (2016). *Anal. Chem.* **88**, 11982–11985.
Zhu, G. B., Wang, S. Y., Wang, Y., Wang, C. X., Risgaard-Petersen, N., Jetten, M. S. M. & Yin, C. Q. (2011). *Isme J.* **5**, 1905–1912.